



High-strength porous biomaterials for bone replacement: A strategy to assess the interplay between cell morphology, mechanical properties, bone ingrowth and manufacturing constraints



Sajad Arabnejad^a, R. Burnett Johnston^a, Jenny Ann Pura^b, Baljinder Singh^a, Michael Tanzer^c, Damiano Pasini^{a,*}

^a Mechanical Engineering Department, McGill University, Montreal, Quebec H3A0C3, Canada

^b Department of Experimental Surgery, Montreal General Hospital, McGill University, Montreal, Quebec H3G1A4, Canada

^c Jo Miller Orthopaedic Research Laboratory, Division of Orthopaedics, Montreal General Hospital, McGill University, Montreal, Quebec H3G1A4, Canada

ARTICLE INFO

Article history:

Received 25 June 2015

Received in revised form 26 October 2015

Accepted 29 October 2015

Available online 30 October 2015

Keywords:

Porous biomaterials

Lattice materials

Mechanical properties

Bone ingrowth

Additive manufacturing

ABSTRACT

High-strength fully porous biomaterials built with additive manufacturing provide an exciting opportunity for load-bearing orthopedic applications. While factors controlling their mechanical and biological response have recently been the subject of intense research, the interplay between mechanical properties, bone ingrowth requirements, and manufacturing constraints, is still unclear. In this paper, we present two high-strength stretch-dominated topologies, the Tetrahedron and the Octet truss, as well as an intuitive visualization method to understand the relationship of cell topology, pore size, porosity with constraints imposed by bone ingrowth requirements and additive manufacturing. 40 samples of selected porosities are fabricated using Selective Laser Melting (SLM), and their morphological deviations resulting from SLM are assessed via micro-CT. Mechanical compression testing is used to obtain stiffness and strength properties, whereas bone ingrowth is assessed in a canine *in vivo* model at four and eight weeks. The results show that the maximum strength and stiffness ranged from 227.86 ± 10.15 to 31.37 ± 2.19 MPa and 4.58 ± 0.18 to 1.23 ± 0.40 GPa respectively, and the maximum 0.2% offset strength is almost 5 times stronger than that of tantalum foam. For Tetrahedron samples, bone ingrowth after four and eight weeks is $28.6\% \pm 11.6\%$, and $41.3\% \pm 4.3\%$, while for the Octet truss $35.5\% \pm 1.9\%$ and $56.9\% \pm 4.0\%$ respectively. This research is the first to demonstrate the occurrence of bone ingrowth into high-strength porous biomaterials which have higher structural efficiency than current porous biomaterials in the market.

Statement of significance

We present two stretch-dominated cell topologies for porous biomaterials that can be used for load-bearing orthopaedic applications, and prove that they encourage bone ingrowth in a canine model. We also introduce an intuitive method to visualize and understand the relationship of cell topology, pore size, porosity with constraints imposed by bone ingrowth requirements and additive manufacturing. We show this strategy helps to gain insight into the interaction of exogenous implant factors and endogenous system factors that can affect the success of load-bearing orthopaedic devices.

© 2015 Acta Materialia Inc. Published by Elsevier Ltd. All rights reserved.

1. Introduction

A biomaterial is a synthetic or natural material intended to interface with a biological system [1]. Porous biomaterials constitute a smaller subsection of the whole field of biomaterials and

are particularly relevant for bone interfacing components since they provide a high surface area for bone ingrowth for secondary long term biologic fixation in orthopedic and dental bone implant applications [2]. Porous biomaterials for bone replacement should fulfill specific criteria including: filling bone defect cavities, pore interconnectivity and pore architecture that promote bone formation as well as facilitate the exchange of nutritional components and oxygen to enhance bone ingrowth [3–5], and sufficient

* Corresponding author.

E-mail address: Damiano.pasini@mcgill.ca (D. Pasini).

strength to support physiological loading. In addition, their mechanical properties should ideally be tailored to match the stiffness of the local host bone so as to reduce bone resorption induced by stress shielding [6–9].

Bone ingrowth into an implanted structure is a highly complex phenomenon involving a multitude of factors encompassing a cascade of cellular and extracellular biological events [10]. Among the factors are those that are dependent upon the implanted biomaterial. These include material microarchitecture, e.g. cell topology, porosity, pore shape and size, and properties of the monolithic material among others [11–15]. The function and overall success of a porous biomaterial depend upon the careful selection of a number of morphological parameters, including average pore size and porosity, each affecting the rate of bone ingrowth and interface strength [11,16]. For satisfactory bone ingrowth, porosity should be above 50%, and pore size between 50 and 800 μm [17,18].

For load-bearing applications, porous metallic constructs are predominantly used in bone surgeries because of their severe mechanical strength requirements. A variety of methods have been developed to produce porous metallic scaffolds with a homogeneous pore size distribution that provides a high degree of interconnected porosity for bone ingrowth [2,19]. These processes retain intrinsic limitations, such as an almost uniform distribution of pore size with homogenous porosity. Porous structures with a defined pore shape and size and with a specified porosity distribution, a gradient, or a pattern is very difficult to achieve [20,21]. The thickness of porous coatings might be also insufficient to facilitate effective bone tissue ingrowth [22,23].

Recent advances in additive manufacturing (AM), such as Electron-Beam Melting (EBM) and Selective Laser Melting (SLM), enable to manufacture fully porous structural biomaterials with controlled architecture for bone interfacing applications [17,21,23–26]. AM methods enable scaffolds to be reproduced with controlled topology, porosity, pore shape and size, interconnectivity, and mechanical properties. AM processes allow for the incorporation of gradients of porosity and pore size to tune the performance [20,27]. This allows for a porous biomaterial with an optimum graded microstructure to be designed and manufactured to achieve a desirable mechanical response and functional environment for bone ingrowth.

Among the approaches commonly used to design a porous biomaterial via AM, one consists of selecting the cell topology from a library of unit cells [25,28–30]. The microarchitecture of the unit cell can be tailored to provide sufficient mechanical properties for the porous biomaterial to support physiological loadings with controlled porosity, pore shape, and pore size gradients for an optimum architectural environment for bone ingrowth [15,20,31]. Many studies have shown the use of several AM processes to manufacture unit cells and to evaluate the effect of cell morphology on mechanobiological properties, either *in vitro* and *in vivo* for tissue affinity [24,25,28,32–35]. For implant porous materials, there are currently no quantitative criteria specifying porosity and pore size requirements for bone ingrowth. In particular, there is no study across the length scale that clarifies the role that pore topology, pore size, porosity as well as strut thickness, play in the mechanobiological response of a porous material. The lack of quantitative criteria for understanding such mechanobiological interactions poses challenges to the search of porous materials that can concurrently maximize both mechanical and biological performance. Currently in literature, a common *modus operandi* is to select a cell topology, and with no systematic approach to change iteratively only two of its morphological properties (e.g. cell size, strut thickness, pore size, and porosity) so as to obtain a porous material that is manufacturable. This process, however, does not give a full perspective of the specific property bounds, i.e. the feasible design space, defined by each topology. In addition, this

process often leads to the design of porous materials with pore size range much higher than the optimum range for bone ingrowth [31,35]. Moreover, this procedure does not provide any insight into how the morphological properties of the unit cell, such as unit cell size, pore size, porosity, and strut thickness, are interrelated, and how the change of one parameter can influence the others. Furthermore, to the best of the authors' knowledge, there is also no study that shows how manufacturing and bone ingrowth requirements can affect the admissible design range for a given topology.

This paper presents a systematic methodology for understanding the interplay between the morphological parameters and the mechanobiological properties of structural porous biomaterials. The method enables the generation of design maps where morphological attributes of a given cell topology, such as pore size, porosity, cell size, and strut thickness, are conveniently visualized together with both manufacturing constraints and bone ingrowth requirements. The methodology is applied and demonstrated in this paper with two high-strength topologies: the Tetrahedron and the Octet truss. The cells belong to the class of high-strength and stiffness topologies which are stretch dominated, i.e. their struts axially deform under load [36–43], hence their suitability for load-bearing orthopedic applications. Ti6Al4V representative samples are manufactured via Selective Laser Melting (SLM), and micro-CT analyzed to assess their morphological characteristics with respect to the nominal designed values. Uniaxial compression testing is performed to obtain the effective elastic modulus and yield strength of the manufactured samples. Finally, results from *in vivo* clinical experiments using a canine model are given to assess bone ingrowth after 4 and 8 weeks and to evaluate the potential use of structurally efficient topologies in bone replacement implants.

2. Development of cell topology domains

The mechanical and biological properties of a unit cell for a fully porous biomaterial are governed mainly by the topology, nodal connectivity, porosity, pore size, and the monolithic material from which they are made [22,23,25,34,38,44–46]. The way these morphological parameters are related is not necessarily intuitive; neither is how they affect the mechanical properties and biological response. For this reason, we develop a parametric model to describe the geometry of a unit cell, and subsequently use it to visualize its morphological properties on a design chart. This allows us to visually inspect what porosity and pore size combinations exist and are feasible to manufacture.

As archetype topologies, we select herein the Tetrahedron cell and the Octet truss cell (Fig. 1) and used their parametric geometric models to generate their design domains. From the generalized Maxwell rule for static determinacy [36,41,47], both topologies

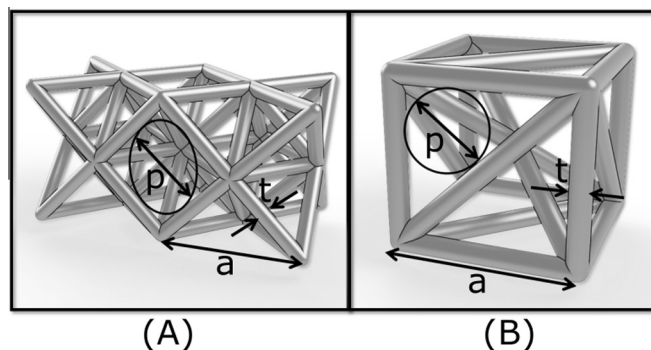


Fig. 1. Parametric models developed for (A) Octet truss unit cell, and (B) Tetrahedron unit cell.

have no internal mechanism in their pin-jointed configuration, which implies that they are stretch dominated for all loading states. The internal forces in both topologies are always axial, either tension and/or compression. For this reason, stretch dominated topologies have higher structural efficiency than those whose struts carry bending. The difference in mechanical properties between the two classes of lattice materials, i.e. stretching versus bending, can be understood with the following example. The strength of a bend dominated cell scales with $\rho^{1.5}$, where ρ is the relative density of the topology [36,38,40], as opposed to the strength of a stretch dominated cell topology which scales with ρ . This means that for a relative density of $\rho = 0.1$, a stretch dominated topology is about three times stronger than a bend dominated topology. A similar reasoning applies for stiffness. In addition, Octet truss and tetrahedron topologies have a stiffness matrix with a cubic symmetry, and they have nearly isotropic mechanical properties [40]. Octet truss has high strength-to-weight ratio which makes it an attractive topology for the design of a high strength porous biomaterial for orthopedic applications. For the tetrahedron lattice, we opt for the non-regular tetrahedron shape, which is the Sommerville # 3 arrangement as described by Goldberg [48], where twelve irregular tetrahedrons are arranged in the form of a cube, which can then be tessellated to completely fill space. The tetrahedron lattice can also conform to complex surfaces and boundaries, and it can easily fill the space of a 3D complex geometry. For these reasons, this work focuses on the mechanobiological investigation of Tetrahedron and Octet truss lattices.

From the geometric analysis of a given topology, a parametric 3D CAD model is created, and used to measure its morphological parameters. The overall cell geometry is controlled by two parameters, strut thickness 't' and unit cell size 'a'. Each unit cell can be scaled through combinations of these parameters to obtain the resultant porosity and pore size. Although there are several methods to define pore size, such as the line intercept and the maximal covering spheres algorithm [49,50], we chose in this work the largest inscribed circle, since in a three dimension generalization it corresponds to the largest sphere that can pass between neighboring cells in a periodic lattice. This measure describes the interconnected pore size for a regular periodic structure, such as the Octet truss and Tetrahedron lattice [51]. The biological relevance is required to allow for the movement of nutrients, waste products and vascularization within the implant which can affect bone ingrowth [13]. Porosity is also measured from the percentage of void in a fully solid cell as:

$$\text{Porosity (\%)} = \left(1 - \frac{V_p}{V_s}\right) \times 100$$

where V_p is the volume of the porous unit cell and V_s is the volume of the fully solid unit cell.

For each cell topology we can obtain and plot the resultant pore size and porosity in contour maps with strut size on the y axis and pore size on the x axis. The values of porosity and cell size are illustrated as isometric lines. The chart can ease the visual understanding of the relation between the morphological parameters of a unit cell. Based on the contours, the following bone ingrowth and manufacturing limits can be superimposed to highlight the admissible design space.

1. Bone ingrowth requirements: pore size between 50 and 800 μm , and the porosity higher than 50% [18,34,52]. These values are included as red lines in the design chart (e.g. Fig. 2).
2. Manufacturing constraints. Most of the current AM technologies, such as SLM and EBM, used to build cellular materials are limited to produce a nominal strut thickness of 200 μm ,

although this limit is process-dependent [21,22,34] and can be lower [53,54]. This limit is included in the design chart with a horizontal red line.

All the designs falling within this domain are acceptable solutions that meet both bone ingrowth requirements and AM limitations. Each unit cell topology is characterized by its own unique design space. To understand how morphological parameters of the unit cells govern the mechanobiological properties of structural porous biomaterials, representative solutions from the admissible region are selected and manufactured to perform mechanical and biological testing, as described in the following sections.

3. Selection and design of representative samples

To experimentally validate the feasibility of a cell topology domain, representative samples are selected and manufactured with SLM for morphological and mechanical investigation. The following criteria are used to select the points from the design domains shown in Figs. 2 and 3 for the Tetrahedron and Octet truss respectively:

- Four design solutions at 50%, 60%, 70% and 75% values of porosity are chosen for each topology to cover the entire porosity range of each cell topology domain. The pore size is also kept constant throughout the relative density range within each topology that corresponds to the pore size used in the canine model study described later. Tetrahedron-based unit cells have pore size of 500 μm , and the Octet truss unit cells have pore size of 770 μm .
- At each design porosity, the corresponding strut thickness between topologies is prescribed to be identical.

The periodicity and sample sizes are designed according to ISO 13314, and detailed in Table 1 [55]. To perform biological testing, we designed transcortical implants for a canine model study that measures the amount of bone ingrowth in periods of 4 and 8 weeks. Six Tetrahedron and four Octet truss transcortical implants with a cylindrical shape and an outer diameter of 5 mm and a height of 10 mm were manufactured using SLM process. The manufactured Tetrahedron topology had an average porosity of 55.51% and pore size of 438 μm . The manufactured Octet truss had an average porosity of 69.88% and pore size of 772 μm . The values of porosity and pore size fall within their admissible design space that accounts for bone ingrowth constraints.

3.1. Manufacturing

The samples were produced using the SLM process by the Renishaw AM250 with building direction as shown in Fig. 4. A 200 W laser with energy density of 60 J/mm³ and laser spot diameter of 70 μm was used for manufacturing, with point by point exposure. Particles ranged from 15 to 50 μm and the layer thickness was 30 μm . The parts were processed at 720° under argon for 2 h, and were removed from the build plate post treatment using EDM wire cutting.

3.2. Morphological investigation

From each design point in the design space (Table 1), one sample was randomly selected and scanned using a SkyScan 1172 high-resolution micro-CT. During the acquisition, each sample was rotated over 360° in steps of 0.5°, using 103 kV energy and

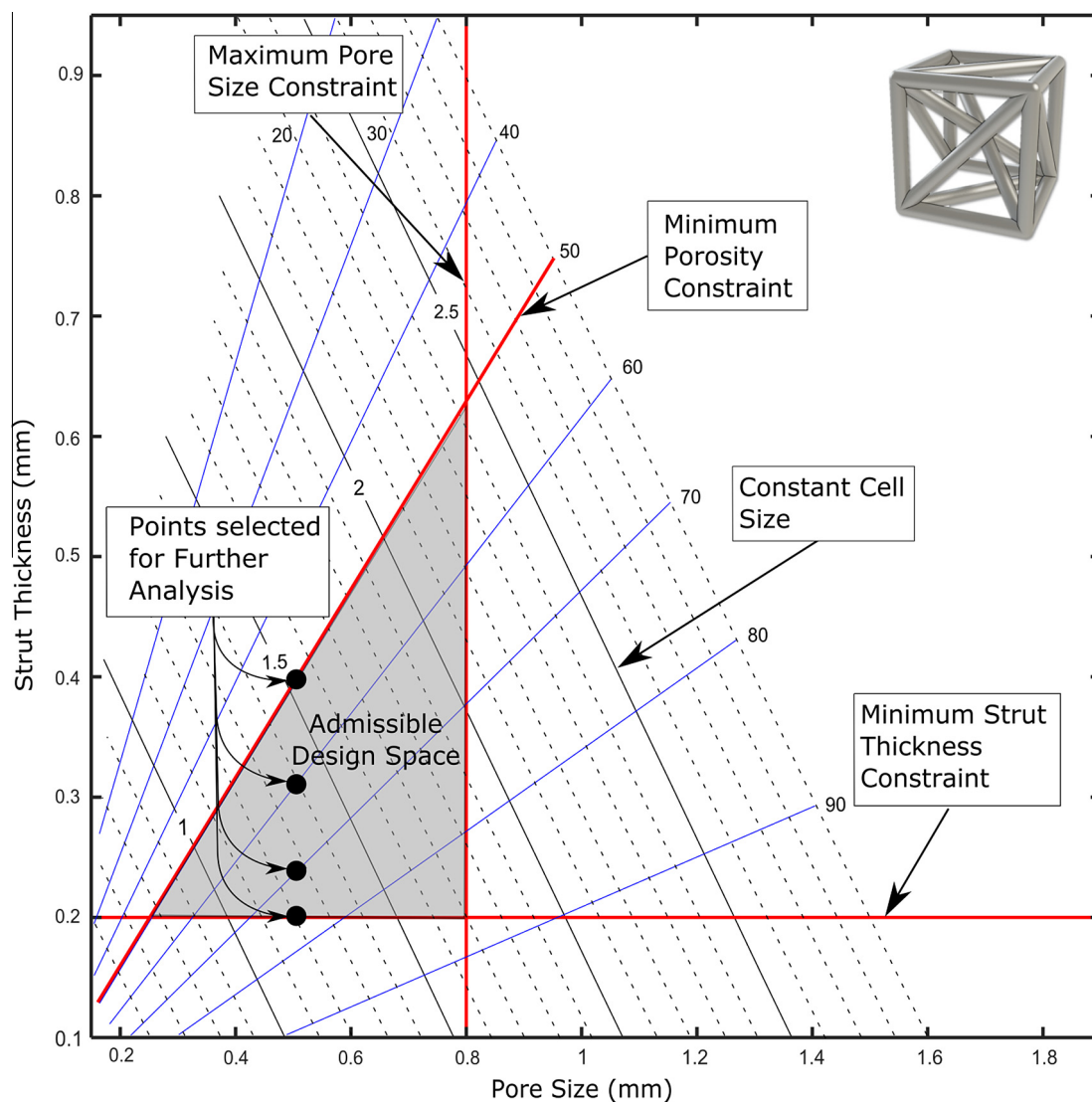


Fig. 2. Design space for tetrahedron topology, with imposed constraints of manufacturing, pore size, and porosity.

96 μA intensity. After each rotation step, 5 images were acquired and the average radiograph recorded. The images were then reconstructed into cross-sectional images with a commercial software package (NRecon, Skyscan N.V., Kontich, Belgium). Using this dataset, a series of image slices were taken from within the build plane and orthogonal to the build plane. Based on the image slices, the strut thickness and pore size were measured with the ImageJ software package (National Institutes of Health, Bethesda, MD) to correspond with the values defined in Fig. 1. Additionally, strut thickness measurements taken orthogonal to the build plane were divided based on the designed strut angle to capture manufacturing discrepancies outside of the build plane. To measure the porosity of the remaining 5 replicates, the samples were weighed and normalized by their bounding dimension volume.

3.3. Compression testing

For the compression testing of samples, a 50 kN MTS servo-electric testing machine was used. Five replicates for each design solution were tested. The samples are compressed with a constant strain rate of 0.01 s^{-1} . The stiffness, yield and ultimate strength of the each sample were determined from the stress–strain curves. The ISO-13314 standard was followed to determine the sample

stiffness as the maximum slope of the stress–strain curve. The yield strength was measured using the 0.2% offset method based on the maximum stiffness, and the first maximum compressive strength was also recorded.

3.4. Bone ingrowth study, surgical protocol and histology

The historical protocol for the canine femoral transcortical implant model by Bobyn et al [11,12] was precisely followed. The animal study protocols were approved by the institution's ethical review committee in accordance with the Canadian Council on Animal Care. The placements of the implants were guided into unicortical holes that were drilled into the lateral cortices of canine femora. Six Tetrahedron and four Octet truss transcortical implants were used for the implantation (Fig. 5). For this pilot study, two healthy, skeletally mature mongrel dogs weighing between 30 and 35 kg were operated on using the following institution-approved protocol. Four weeks after the index procedure on one femur, the procedure was repeated on the contralateral femur.

Both dogs were sacrificed at 8 weeks following the initial surgery, thereby yielding both 4 and 8-weeks ingrowth data for each dog. The harvested femora were divided into separate segments for histological analysis of the bone–implant interface. This involved

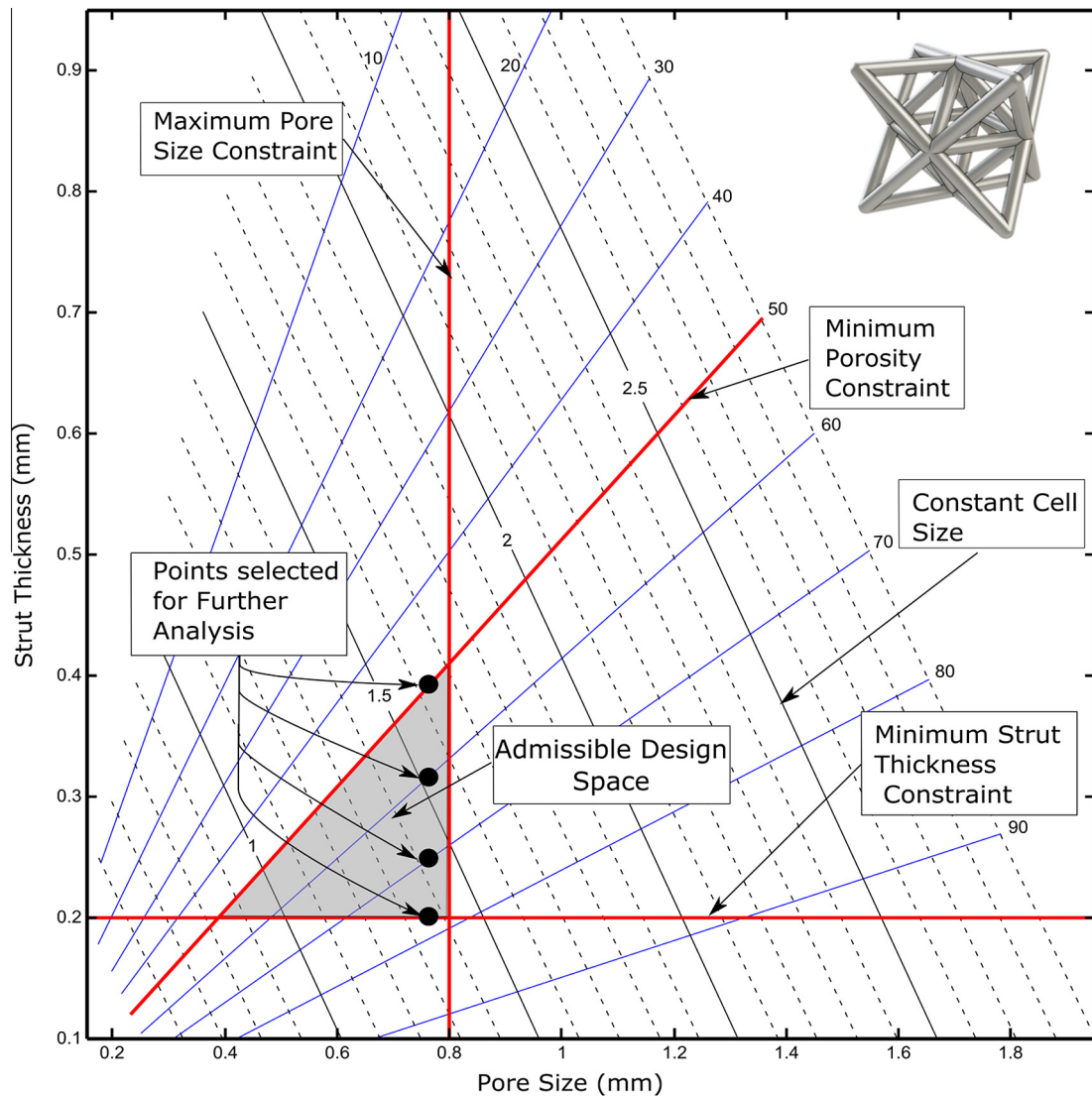


Fig. 3. Design space for Octet truss, with imposed constraints of manufacturing, pore size, and porosity.

Table 1
Geometric details of the test samples.

Unit cell	#	Porosity (%)	Strut thickness (mm)	Unit cell size (mm)	Pore size (mm)	Height (mm)	Width (mm)	Depth (mm)
Tetrahedron	1	50	0.39	1.52	0.5	20.15	12.55	12.55
	2	60	0.31	1.39	0.5	18.31	11.39	11.39
	3	70	0.24	1.27	0.5	16.75	10.40	10.40
	4	75	0.20	1.20	0.5	15.80	9.80	9.80
Octet truss	1	50	0.4	1.66	0.77	21.98	13.68	13.68
	2	60	0.32	1.54	0.77	20.34	12.64	12.64
	3	70	0.25	1.44	0.77	18.97	11.77	11.77
	4	75	0.20	1.37	0.77	18.01	11.16	11.16

dehydrating in ascending solutions of ethanol, defatting in a 1:1 solution of ether-acetone, infiltration under vacuum and embedding with polymethylmethacrylate, and sectioning the implant transversely with a low-speed diamond cut-off apparatus (Buehler, Lake Bluff, IL, USA).

The grayscale-computerized images obtained from BSEM underwent analysis with the program ImageJ software version 1.47 (National Institutes of Health, Bethesda, MD) to detect and quantify bone ingrowth. An in-house code was used to best differentiate bone and the implant, and the amount of bone was

measured from the percentage of grey color with respect to the void space.

4. Results

4.1. Cell morphology: designed vs manufactured

Using micro-CT analyses, the key morphological parameters, including porosity, pore size, and strut thickness, of the samples were measured and compared with the nominal (designed) values.

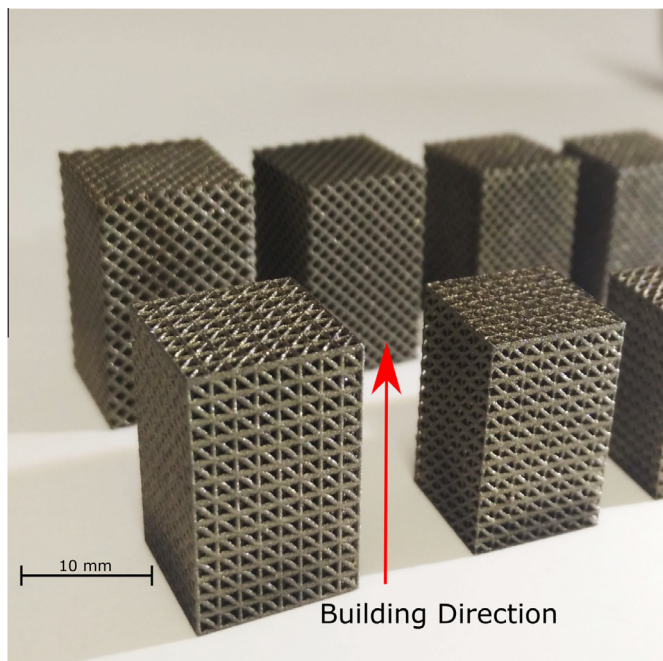


Fig. 4. Vector showing the build direction.

Fig. 6 shows the comparison between designed and measured values for the Tetrahedron and Octet truss lattices. The error between designed and manufactured porosity increases with the increase of the designed porosity. For the Tetrahedron lattice, the difference reaches up to 15% at the highest porosity of 75%. Furthermore, there is consistency among the porosity values measured for each sample, another factor indicating that no major discrepancies exist between the replicates.

Fig. 6c and d show the comparison between the designed value of strut thickness and the average value measured on the manufactured samples. From micro-CT analyses, we observed that strut thickness variation is dependent on the strut angle with respect to the build plane. Fig. 6c and d clearly show that struts measured at 0 degree with respect to the building plane are significantly thicker ($255 \pm 60 \mu\text{m}$) than their designed values due to strut overmelting. However, in the building plane, the thickness of the manufactured struts is in good agreement with the designed values ($35 \pm 37 \mu\text{m}$). This leads to the manufacturing of struts with elliptical cross section with major axis along the building direction and minor axis in the building plane. For struts that are normal to the building plane, the manufactured thickness is slightly lower than that of the designed sample ($-90 \pm 37 \mu\text{m}$), and only reported for the Tetrahedron since Octet truss has no vertical struts. The struts

aligned at $\pm 45^\circ$ had a significantly smaller error than the struts at zero degrees, and even more than the struts aligned in the build direction ($61 \pm 52 \mu\text{m}$).

Measured pore sizes are all lower than the designed values, with deviation between designed and manufactured pore size increasing as the porosity increases. Fig. 6e shows that the average pore size deviation for the Tetrahedron lattice increases from 15% to 32% for designed porosity of 50% to 75%. For Octet truss, we can see in Fig. 6f this deviation increases from 21% to 50% for designed porosity of 50–75%.

4.2. Mechanical properties

Fig. 7 shows the representative stress–strain curve of an Octet truss lattice at 50% porosity. As can be seen, the compressive stress–strain curve can be divided into three main regions: linear elastic, plateau, and densification. The EDM removal of the samples from the build plate results in a slight distortion at the edge of the part. The initial non-linear phase of the stress strain curve is a result of these small uneven struts yielding locally [56,57]. To calculate the stiffness and yield strength, this initial nonlinear behavior has been disregarded in the subsequent analysis of the data. Sample stiffness is obtained from the maximum value of stress–strain slope in the linear elastic region, and their yield strengths are obtained from 0.2% offset method. The results are presented in Table 2.

The values of stiffness and yield strength are compared in Fig. 8 for Tetrahedron and Octet trusses. For the Tetrahedron topology, stiffness and strength of the lattice samples decrease with increasing porosity. Octet truss shows similar decrease up to a design porosity of 70%, with no decrease in strength at 75% designed porosity. At a low designed porosity of 50%, the Octet truss is stronger and stiffer than the Tetrahedron. However, as the porosity increases, the trend reverses, with the strength and stiffness of the Tetrahedron much higher than that of Octet trusses.

4.3. Bone ingrowth: histology

Bone ingrowth was observed in all implants at both the 4 and 8 week time periods (Fig. 9). At 4 weeks, there was new bone forming at the implant–cortical interface. At 8 weeks, new bone had grown within the implant and completely filled the porous structure adjacent to the cortices. In addition, bone ingrowth was present in the portion of the implant that was within the cancellous medullary canal. Qualitatively, the backscattered SEM images demonstrated that the bone formed in and around the implants was structurally similar in gross appearance to native trabecular bone. Neither a histological comparison nor quantitative comparison of mineralization between native bone and newly formed peri-implant bone was performed.

The amount of bone ingrowth at 4 weeks for Tetrahedron and Octet truss implants were $28.6\% \pm 11.6\%$ and $35.5\% \pm 1.9\%$, respectively. At 8 weeks, bone ingrowth increased to $41.3\% \pm 4.3\%$ and 56.9% for both respective implants. The Octet truss implant shows more bone ingrowth compared to Tetrahedron implant at both time points.

5. Discussion

5.1. Discrepancy between manufactured and designed samples

The design charts do not exactly predict the measured porosity and pore size of the manufactured samples. The reason can be attributed to deviations between a designed sample and its manufactured counterpart. A key factor is the deviation observed in the

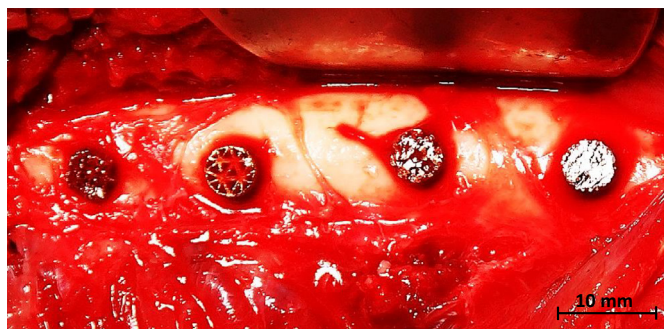


Fig. 5. Intraoperative photograph illustrating four femoral transcortical implants positioned perpendicular to the lateral femoral cortex.

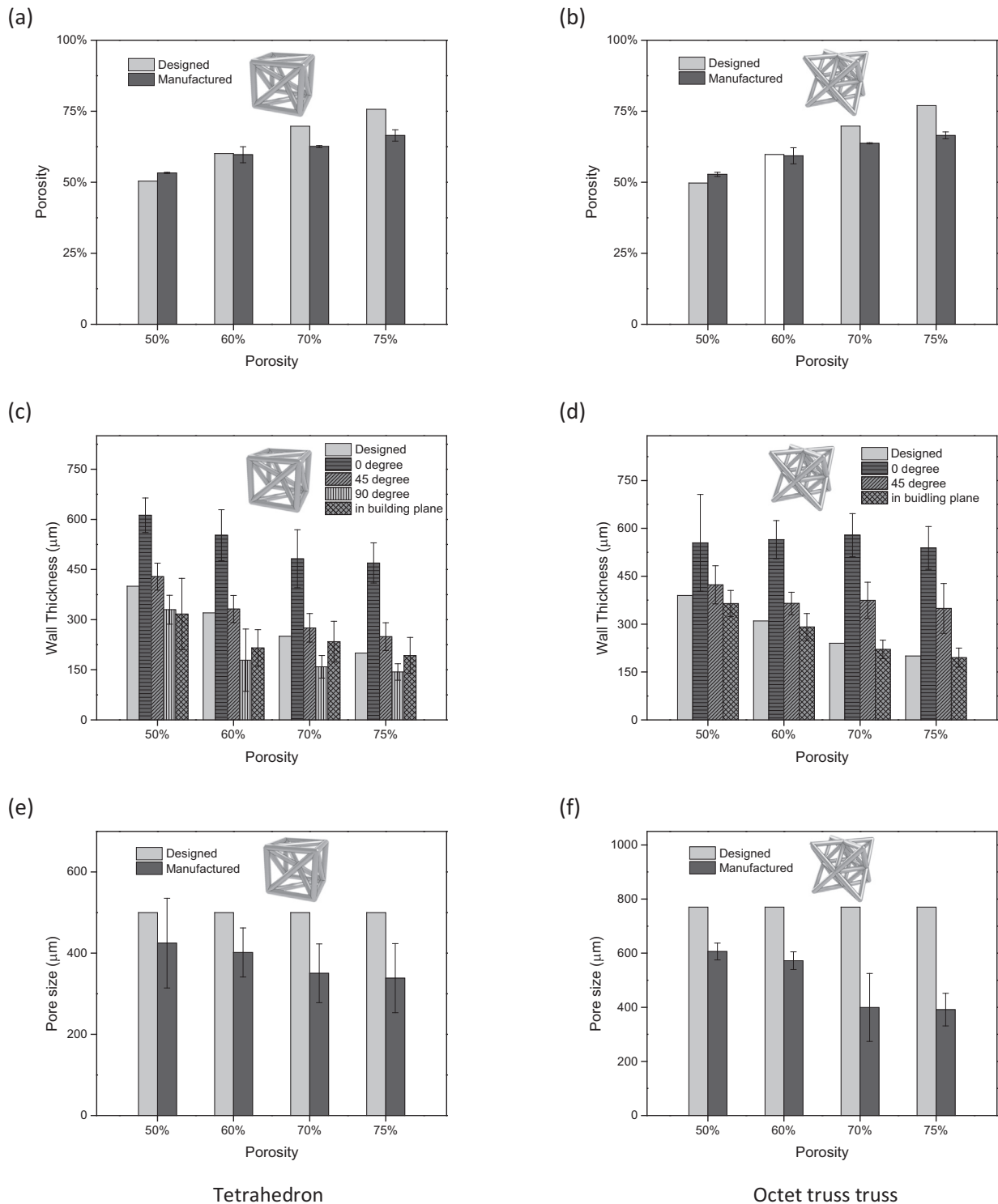


Fig. 6. Average porosity, strut thickness, and pore size of Tetrahedron and Octet truss lattices. Values obtained via micro-CT image analysis and compared to the respective designed geometries.

strut thickness and strut cross section between manufactured and designed samples. The measured error for the strut thickness was dependent on the angle a strut forms with respect to the building plane; this error was most apparent in overhanging horizontal struts. Due to the overmelting out of the build plane, the strut cross section is no longer circular and it changes to ellipse. Variations of strut thickness as a function of the angle with respect to the building plane is well documented in the literature, and can be

attributed to the difference in heat transfer properties between solid struts and surrounding powder [35,58]. The increase of strut thickness leads to a decreased porosity and pore size in the manufactured samples.

To highlight the manufacturing discrepancies, a representative unit cell from manufactured sample was reconstructed and overlaid with the designed unit cell. Fig. 10 shows 3D reconstructed a Tetrahedron unit cell at porosity of 75%, which are overlaid with

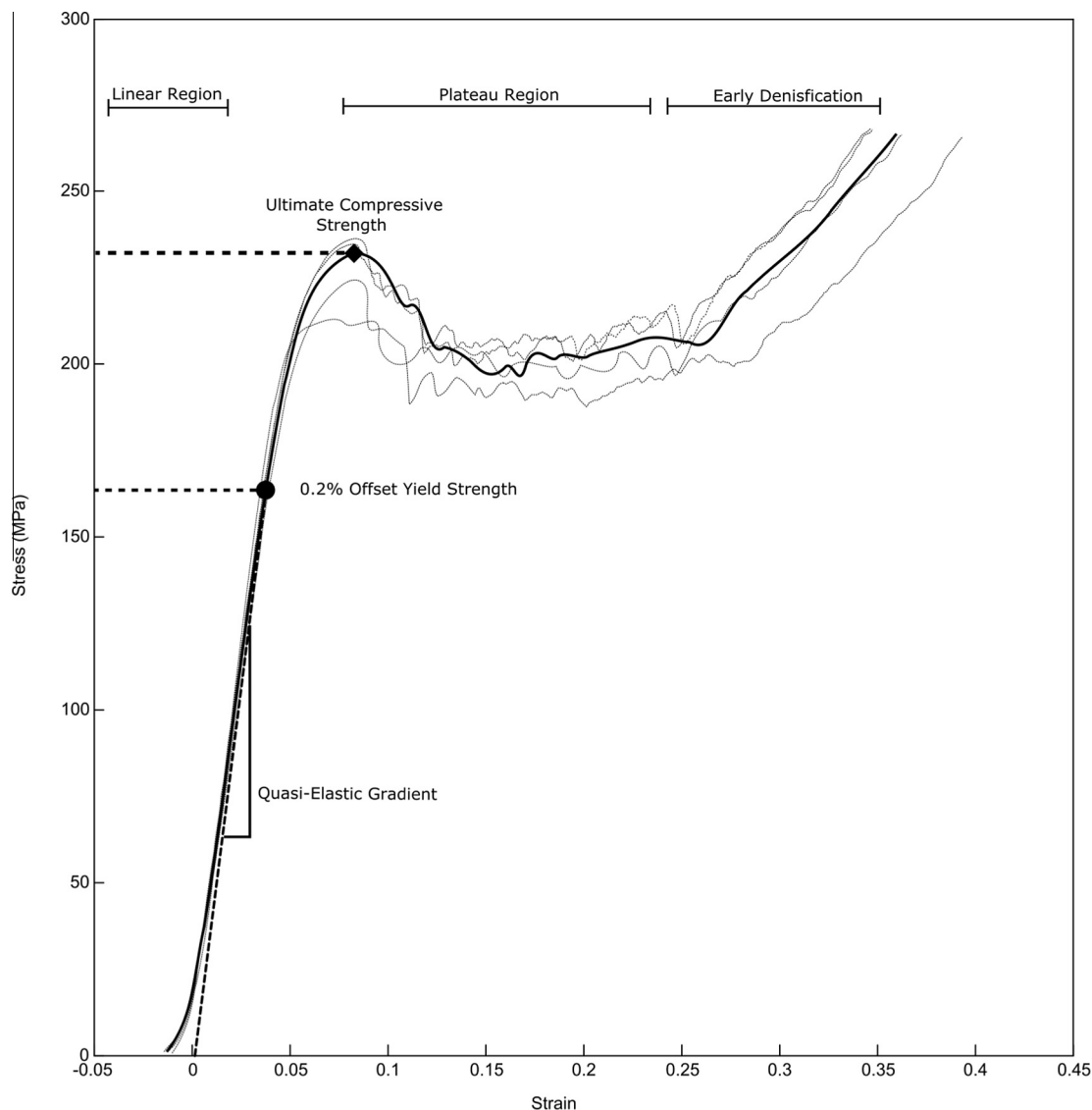


Fig. 7. Compressive stress strain of a representative Octet truss at 50% porosity. The graph shows a clear difference between the 0.2% offset yield strength and the ultimate compressive strength.

Table 2
Mechanical properties of Tetrahedron and Octet truss samples.

Designed porosity	Stiffness (GPa)			0.2% offset strength (MPa)			First maximum strength (MPa)		
	Tetrahedron	Octet truss	<i>P</i> value	Tetrahedron	Octet truss	<i>P</i> value	Tetrahedron	Octet truss	<i>P</i> value
50	4.3 ± 0.1	4.6 ± 0.2	0.029	156 ± 6	172 ± 8	0.0063	219 ± 8	228 ± 10	0.19
60	3.1 ± 0.4	3.4 ± 0.3	0.18	99 ± 17	119 ± 22	0.14	136 ± 23	145 ± 34	0.6
70	2.9 ± 0.1	1.4 ± 0.2	1.20E–06	88 ± 4	31 ± 2	1.30E–07	120 ± 4	31 ± 2	2.50E–09
75	1.9 ± 0.1	1.2 ± 0.4	0.015	57 ± 8	34 ± 11	0.008	68 ± 3	39 ± 3	1.40E–05

their designed counterparts. The figure shows that the strut thickness of manufactured samples is sensibly higher than the designed ones. At the corners, we also note material agglomeration, leading to a fillet-like feature. Comparing to Fig. 6A and B, we observe the discrepancy of manufactured porosity and pore size increases with the porosity. This trend can be attributed to the absolute error of the strut thickness, which is nearly constant for all the designed strut thicknesses. The relation between the increase in strut thickness and decrease in porosity can be intuitively understood by examining the design charts. If the wall thickness is increased for a given cell size, it reaches regions with a lower porosity and pore

size. This variation in porosity for a given strut thickness change is more severe for smaller unit cells.

5.2. Strategies to minimize the differences between the design chart predictions and the manufacturing outcomes

To minimize the difference between the predicted properties, as visualized in the design charts, and the manufacturing outcomes, two methods can be pursued. The first, obvious, although non-trivial, is to reduce the manufacturing error. This procedure can potentially be implemented through machine parameter tuning,

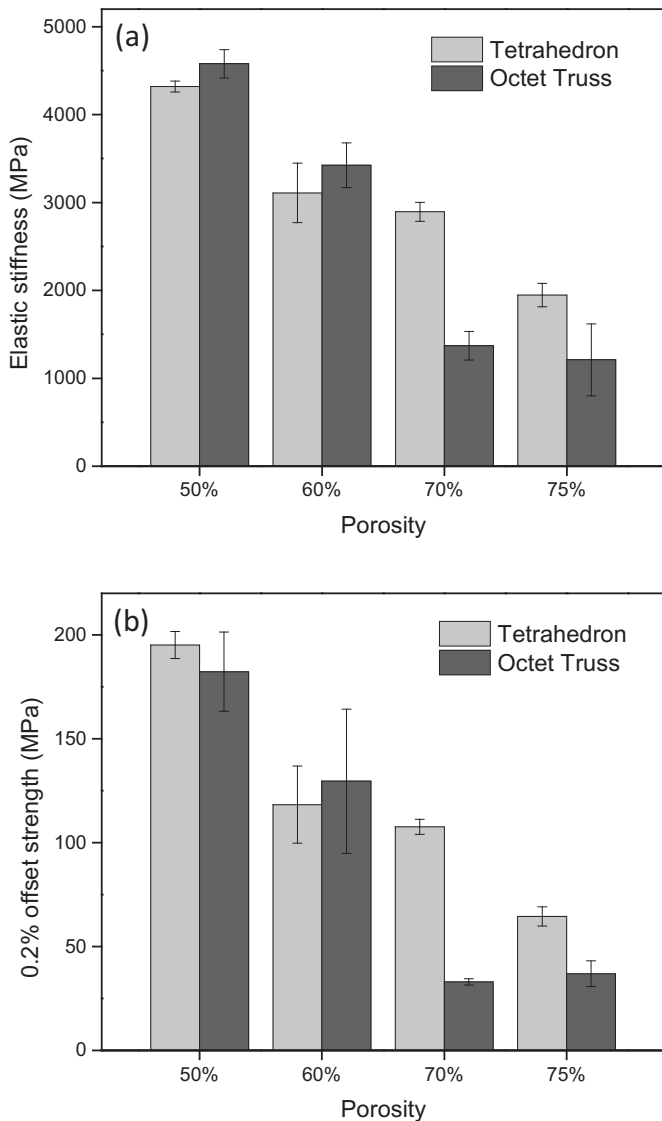


Fig. 8. (a) The Young's-modulus and (b) the compressive yield strength of Tetrahedron and Octet truss lattice as a function of designed and measured porosity.

post-processing, such as acid etching and electro polishing, and design compensation strategies [59]. The additional post-process can have a substantial effect on the mechanical properties, and biological performance [21,60]. A second method is to incorporate the manufacturing errors into the geometrical model used to create the design charts. This strategy enables one to visualize the properties of the manufactured samples on the charts, thereby accounting for any variation in the strut cross-sectional profile and thickness throughout the unit cell. The design charts, therefore, could capture the impact that prescribed manufacturing parameters and process errors of a given manufacturing technology might have on the design domain of a given cell topology.

5.3. Mechanical properties

Fig. 11 shows the 0.2% compressive strength across the range of all designed porosities for both topologies, and compares it to the strength of tantalum foam, which is extensively used as a coating for bone in growth in orthopedic applications [61]. The strength of tantalum foam is extracted from the study performed by

Zardiackas et al. [61] on metallurgy and mechanical characterization of tantalum foams with porosity between 75% and 85%. The tetrahedron is stronger than the tantalum foam at all designed porosities, with 50% porosity almost 5 times stronger. Octet truss at 50% and 60% design porosity exhibits higher strength compared to the stochastic foam. However, the Octet truss lattice at high porosity shows a sudden drop in mechanical properties. One cause may be the smaller average strut dimensions for the Octet truss samples at high porosity. Previous studies indicated a dependency on strut thickness in addition to porosity, with thinner struts resulting in lower strength even at constant porosity [24]. The decrease in stiffness and strength with decreasing thickness contrasts to the findings of Yan et al. [57], who found that samples with equal porosity but larger cell size (and hence strut size) had decreased strength and stiffness. For both of the topologies tested in this paper, the strut thickness and porosity are equivalent. However, the strength of the Tetrahedron at high porosity (70% designed) is significantly higher (87.85 ± 4.23 vs. 30.96 ± 2.10 MPa, $P = 1.3 \times 10^{-7}$). At high porosity, the stiffness of the Tetrahedron is also higher than that of the Octet truss (2.89 ± 0.12 GPa vs. 1.37 ± 0.18 GPa, $P = 1.3 \times 10^{-6}$). This is in contrast to the lowest 50% porosity design where the Octet truss is both stronger and stiffer than the Tetrahedron. This drastic decrease in strength and stiffness at high porosity could be attributed to manufacturing defects that could potentially lead to a change in the mechanism of deformation. The manufactured Octet truss sample would no longer be dominated by strut stretching, rather by a failure mode dominated by bending. Other phenomena, such as geometric size effect due to local variations in alloy microstructure and mechanical anisotropy of the SLM alloy, could also contribute to the drastic decrease of stiffness and strength of the Octet truss at high porosity. While further study is required, the experimental data obtained in this work show that at high values of porosity and for strut thickness near to

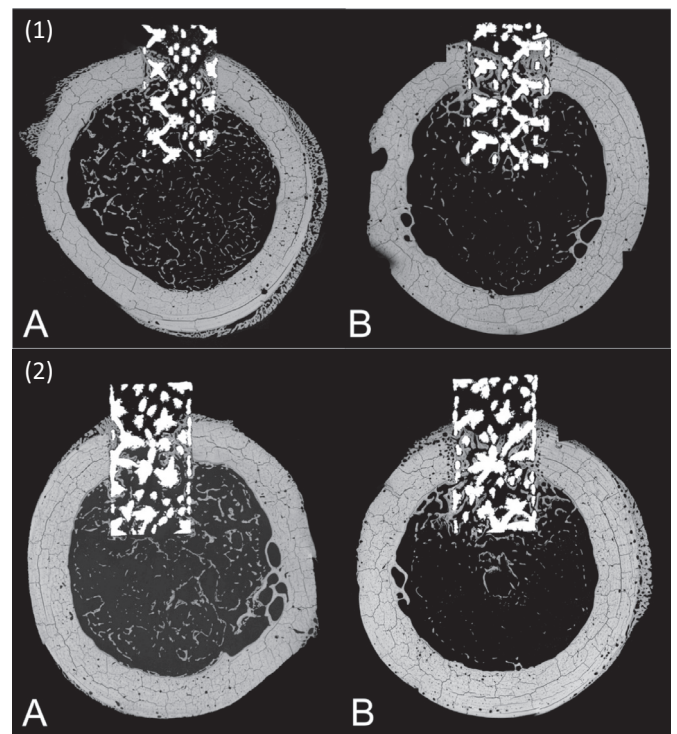


Fig. 9. Backscattered scanning electron micrograph of a transverse (1) Octet truss and (2) Tetrahedron transcortical implant section at (A) 4 weeks, and (B) 8 weeks. Bone ingrowth is throughout the length of the implant at the 8 week time point.

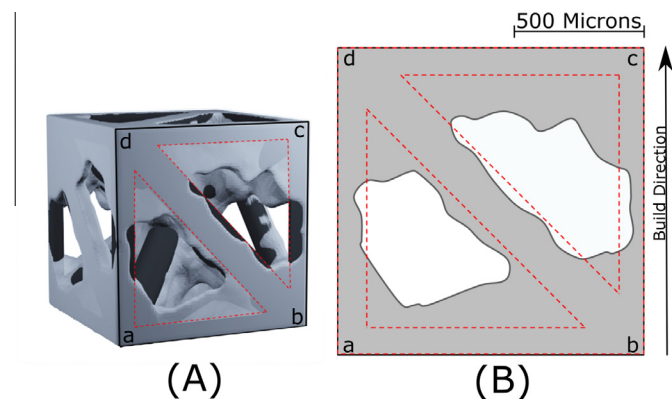


Fig. 10. (A) Reconstructed Tetrahedron cell at 75% porosity from CT (translucent grey) overlaid with designed unit cell (black). (B) Front view (abcd) of the cell with the designed geometry outlined in red dashed lines. The over melting of horizontal struts, the staircase effect on struts at 45°, and the under sizing of the vertical struts are shown. (For interpretation of the references to color in this figure legend, the reader is referred to the web version of this article.)

the manufacturing limits, the Octet truss is more sensitive to manufacturing errors than the Tetrahedron lattices.

5.4. Bone ingrowth

The *in vivo* canine study results are part of a pilot study that aims to assess the biological performance of highly porous structural biomaterials with a stretch-dominated mechanical behavior:

Octet truss and Tetrahedron based. The primary goal is to determine if bone ingrowth occurs within stretch-dominated lattices manufactured with SLM. The *in vivo* studies clearly demonstrate that bone ingrowth occurs in all implants in a reproducible and predictable fashion. Both topologies demonstrate early and extensive bone ingrowth by 4 weeks, averaging 29% and 36% for the Tetrahedron and Octet truss respectively. By 8 weeks' time, there is a further 41% and 58% increase in bone ingrowth for the Tetrahedron and Octet truss topologies.

We provide a comparison with some porous coatings currently used in orthopedic implants, including Trabecular Metal (TM) and tantalum foam [12,62,63]. Four and six week canine studies have shown that the amount of bone ingrowth into these porous coating varies between about 15% to 50% [62,63], while for TM, the amount of ingrowth is higher and increases from 13% in two week to 53% in four weeks [12]. As can be seen in Table 3, we found that the amount of bone ingrowth for Tetrahedron and Octet truss samples is lower than TM but in the range of other porous coatings. Studies have shown that the amount of bone ingrowth is linearly proportional to the porosity of sample. One of the main advantages of the tested samples compared to TM is their increased mechanical strength. Because these samples are manufactured with additive manufacturing, the porosity gradient can be tightly tailored to minimize stress shielding while maintaining sufficient strength for a fully porous implant application. In addition, the high-strength porous structures can be manufactured with an interface layer that has optimal pore size and porosity for bone ingrowth, whereas the internal microstructure can be designed to feature lower porosity, resulting in high mechanical strength to support

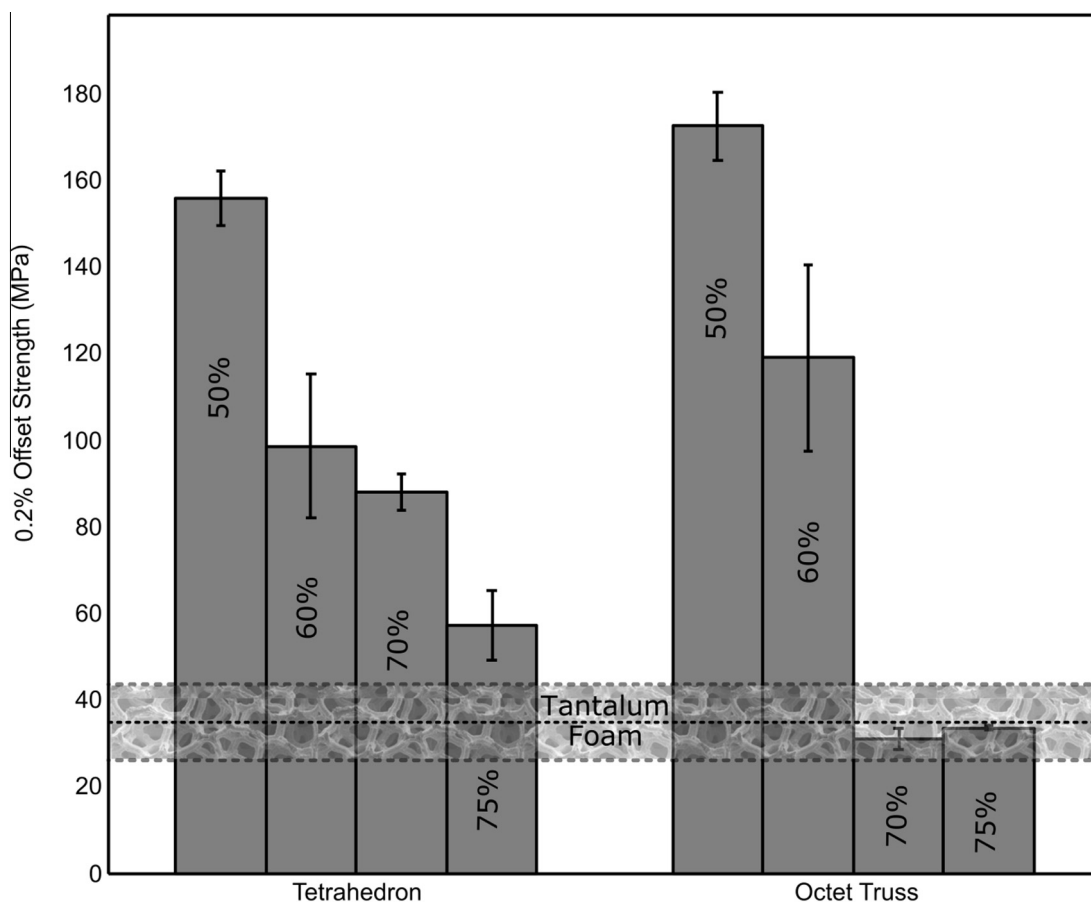


Fig. 11. Comparison of mechanical 0.2% offset strength of the structural porous biomaterials examined in this work and that of tantalum foam; the horizontal bound is the average and deviation of tantalum foam under quasi static compression [61].

physiological loadings. The bone ingrowth results are encouraging and require further corroboration to understand the impact of cell topology, pore size and porosity on bone ingrowth.

While this work might pave the way to the use of stretch-dominated cell topologies in reconstructive orthopedics, there are opportunities for improvement in future studies. A primary limitation is the use of mass and volume porosity measurements that have served as a surrogate to a detailed CT analysis of each of the individual test samples. This means that potential defects that could have a large effect on mechanical properties, other than porosity, were not captured. In addition, this choice also restricts the analysis of intra-batch variation between samples. Another limitation is that our samples were mechanically tested only in compression. For load bearing orthopedic applications, there are multiple stress states including compression, tension, bending and torsion, in addition to repetitive cyclical fatigue loading. This scenario is critically important, since some topologies, such as the cube can be very strong in compression along the strut orientation, but have their strength drop if a macroscopic shear load is applied to the samples [64]. Further work is required to examine their efficiency for other loading cases. In the current study, no finite element simulation was used to predict the mechanical properties of these two topologies. Computational predictions are part of a parallel work currently underway, which aims at providing a comprehensive mechanical characterization of Octet truss and Tetrahedron topologies throughout the entire design space. The impact of cell size, mechanical anisotropy, and manufacturing defects, including waviness of cell struts, variation of strut thickness, and agglomeration of semi melted beads on cell struts are investigated. Another limitation in the analysis of bone ingrowth is that the percentage of ingrowth into the implant is dependent on the section that was prepared for SEM analysis. Because the analysis is performed on a planar section, the ingrowth percentage is two dimensional in nature, and representative - but not an exact -measure of the volume of new bone within the porous material.

6. Conclusions

We have presented two stretch-dominated cell topologies for porous biomaterials that can be used for load-bearing orthopedic applications, and proven that they encourage bone ingrowth in a canine model. We also presented an intuitive method to visualize and understand the pore size and porosity as a function of the design variables governing a porous material. Furthermore, it was shown how bone ingrowth and manufacturing constraints can be easily integrated into cell topology domains that allow for a holistic understanding of the interplay between cell geometry, mechanical properties, bone ingrowth and manufacturing errors, each factor controlling the design of a porous biomaterial for bone replacement. This scheme can be used to visually compare the design domains of other cell topologies, each with its manufacturing constraints, bone ingrowth rate and mechanical properties, all in one chart. The strategy can help to further clarify the interaction of exogenous implant factors and endogenous system factors that can affect the success of load-bearing orthopedic devices.

Table 3

Mean values and standard deviations of bone ingrowth at 4 and 8-week intervals for Tetrahedron and Octet truss transcortical implants. The implant porosity values were measured via microCT analysis.

Time period (weeks)	Topology	Porosity (%)	Bone ingrowth
4	Tetrahedron	55.5	28.6% ± 11.6%
	Octet truss	69.9	35.5% ± 1.9%
8	Tetrahedron	55.5	41.3% ± 4.3%
	Octet truss	69.9	56.9% ± 4.0%

Results from micro CT analysis have shown geometry deviations between the designed samples and the manufactured samples, discrepancies that can be predominantly attributed to the strut overmelting, which depends on the strut orientation. Manufacturing inaccuracy leads to a reduction of the porosity and pore size that can be obtained with a given additive manufacturing technology, in this case SLM. Mechanical testing also confirmed the role of porosity on mechanical properties. We have shown that Octet truss samples at high porosity and small cell size are sensitive to manufacturing errors. Work is currently underway to minimize the geometric variation between designed and manufactured samples, as well as the introduction of additional parameters to the design charts, such as iso-permeability lines, mechanical properties values, and bone ingrowth performance. These will all contribute to capturing the tradeoff among structural, manufacturing, biological and mechanical requirements for porous bone replacement materials.

Acknowledgment

The authors acknowledge the financial support from the Natural Sciences and Engineering Research Council of Canada (NSERC) and the Canadian Institutes of Health Research (CIHR).

References

- [1] L.S. Nair, C.T. Laurencin, Biodegradable polymers as biomaterials, *Prog. Polym. Sci.* 32 (2007) 762–798.
- [2] B. Levine, A new era in porous metals: applications in orthopaedics, *Adv. Eng. Mater.* 10 (2008) 788–792.
- [3] S.J. Hollister, W.L. Murphy, Scaffold translation: barriers between concept and clinic, *Tissue Eng. Part B: Rev.* 17 (6) (2011) 459–474.
- [4] G.H. Billström, A.W. Blom, S. Larsson, A.D. Beswick, Application of scaffolds for bone regeneration strategies: current trends and future directions, *Injury* 44 (2013) S28–S33.
- [5] S. Wu, X. Liu, K.W. Yeung, C. Liu, X. Yang, Biomimetic porous scaffolds for bone tissue engineering, *Mater. Sci. Eng.: R: Rep.* 80 (2014) 1–36.
- [6] S.A. Khanoki, D. Pasini, Multiscale design and multiobjective optimization of orthopedic hip implants with functionally graded cellular material, *J. Biomech. Eng.* 134 (2012) 031004.
- [7] S.A. Khanoki, D. Pasini, The fatigue design of a bone preserving hip implant with functionally graded cellular material, *J. Med. Devices* 7 (2013) 020907.
- [8] J. Bobyn, E. Mortimer, A. Glassman, C. Engh, J. Miller, C. Brooks, Producing and avoiding stress shielding: laboratory and clinical observations of noncemented total hip arthroplasty, *Clin. Orthop. Relat. Res.* 274 (1992) 79–96.
- [9] A. Glassman, J. Bobyn, M. Tanzer, New femoral designs do they influence stress shielding?, *Clin. Orthop. Relat. Res.* 453 (2006) 64–74.
- [10] M. Fini, G. Giavaresi, P. Torricelli, V. Borsari, R. Giardino, A. Nicolini, et al., Osteoporosis and biomaterial osteointegration, *Biomed. Pharmacother. Biomed. Pharmacother.* 58 (2004) 487–493.
- [11] J. Bobyn, R. Pilliar, H. Cameron, G. Weatherly, The optimum pore size for the fixation of porous-surfaced metal implants by the ingrowth of bone, *Clin. Orthop. Relat. Res.* 150 (1980) 263.
- [12] J. Bobyn, G. Stackpool, S. Hacking, M. Tanzer, J. Krygier, Characteristics of bone ingrowth and interface mechanics of a new porous tantalum biomaterial, *J. Bone Joint Surg. Br.* 81 (1999) 907–914.
- [13] A.C. Jones, C.H. Arns, D.W. Hutmacher, B.K. Milthorpe, A.P. Sheppard, M.A. Knackstedt, The correlation of pore morphology, interconnectivity and physical properties of 3D ceramic scaffolds with bone ingrowth, *Biomaterials* 30 (2009) 1440–1451.
- [14] J.E. Biemond, R. Aquarius, N. Verdonschot, P. Buma, Frictional and bone ingrowth properties of engineered surface topographies produced by electron beam technology, *Arch. Orthop. Trauma Surg.* 131 (2011) 711–718.
- [15] C.M. Bidan, K.P. Komareddy, M. Rumpel, P. Kollmannsberger, P. Fratzl, J.W. Dunlop, Geometry as a factor for tissue growth: towards shape optimization of tissue engineering scaffolds, *Adv. Healthcare Mater.* 2 (2013) 186–194.
- [16] H. Kienapfel, C. Sprey, A. Wilke, P. Griss, Implant fixation by bone ingrowth, *J. Arthroplasty* 14 (1999) 355–368.
- [17] P. Heintz, L. Müller, C. Körner, R.F. Singer, F.A. Müller, Cellular Ti–6Al–4V structures with interconnected macro porosity for bone implants fabricated by selective electron beam melting, *Acta Biomater.* 4 (2008) 1536–1544.
- [18] C. Bragdon, M. Jasty, M. Greene, H. Rubash, W. Harris, Biologic fixation of total hip implants: insights gained from a series of canine studies, *J. Bone Joint Surg.* 86 (2004) 105–117.
- [19] G. Ryan, A. Pandit, D.P. Apatsidis, Fabrication methods of porous metals for use in orthopaedic applications, *Biomaterials* 27 (2006) 2651–2670.
- [20] J.M. Sobral, S.G. Caridade, R.A. Sousa, J.F. Mano, R.L. Reis, Three-dimensional plotted scaffolds with controlled pore size gradients: effect of scaffold

- geometry on mechanical performance and cell seeding efficiency, *Acta Biomater.* 7 (2011) 1009–1018.
- [21] M. de Wild, R. Schumacher, K. Mayer, E. Schkommodau, D. Thoma, M. Bredell, et al., Bone regeneration by the osteoconductivity of porous titanium implants manufactured by selective laser melting: a histological and micro computed tomography study in the rabbit, *Tissue Eng. Part A* 19 (2013) 2645–2654.
 - [22] L.E. Murr, S.M. Gaytan, E. Martinez, F. Medina, R.B. Wicker, Next generation orthopaedic implants by additive manufacturing using electron beam melting, *Int. J. Biomater.* 2012 (2012).
 - [23] L. Murr, S. Gaytan, F. Medina, H. Lopez, E. Martinez, B. Machado, et al., Next-generation biomedical implants using additive manufacturing of complex, cellular and functional mesh arrays, *Philos. Trans. R. Soc. A: Math. Phys. Eng. Sci.* 368 (2010) 1999–2032.
 - [24] J. Parthasarathy, B. Starly, S. Raman, A. Christensen, Mechanical evaluation of porous titanium (Ti6Al4V) structures with electron beam melting (EBM), *J. Mech. Behav. Biomed. Mater.* 3 (2010) 249–259.
 - [25] L. Mullen, R. Stamp, W. Brooks, E. Jones, C. Sutcliffe, Selective laser melting: a regular unit cell approach for the manufacture of porous, titanium, bone in-growth constructs, suitable for orthopedic applications, *J. Biomed. Mater. Res. B Appl. Biomater.* 89 (2008) 325–334.
 - [26] S. Arabnejad Khanoki, D. Pasini, Fatigue design of a mechanically biocompatible lattice for a proof-of-concept femoral stem, *J. Mech. Behav. Biomed. Mater.* 22 (2013) 65–83.
 - [27] A. Khoda, I.T. Ozbolat, B. Koc, Engineered tissue scaffolds with variational porous architecture, *J. Biomech. Eng.* 133 (2011) 011001.
 - [28] M.A. Wettergreen, B.S. Bucklen, B. Starly, E. Yuksel, W. Sun, M.A.K. Liebschner, Creation of a unit block library of architectures for use in assembled scaffold engineering, *Comput. Aided Des.* 37 (2005) 1141–1149.
 - [29] C. Cheah, C. Chua, K. Leong, S. Chua, Development of a tissue engineering scaffold structure library for rapid prototyping. Part 1: investigation and classification, *Int. J. Adv. Manuf. Technol.* 21 (2003) 291–301.
 - [30] C. Cheah, C. Chua, K. Leong, S. Chua, Development of a tissue engineering scaffold structure library for rapid prototyping. Part 2: parametric library and assembly program, *Int. J. Adv. Manuf. Technol.* 21 (2003) 302–312.
 - [31] S. Van Bael, Y.C. Chai, S. Truscillo, M. Moesen, G. Kerckhofs, H. Van Oosterwyck, et al., The effect of pore geometry on the in vitro biological behavior of human periosteum-derived cells seeded on selective laser-melted Ti6Al4V bone scaffolds, *Acta Biomater.* 8 (2012) 2824–2834.
 - [32] S.J. Li, L.E. Murr, X.Y. Cheng, Z.B. Zhang, Y.L. Hao, R. Yang, et al., Compression fatigue behavior of Ti–6Al–4V mesh arrays fabricated by electron beam melting, *Acta Mater.* 60 (2012) 793–802.
 - [33] S. Arabnejad, D. Pasini, Mechanical properties of lattice materials via asymptotic homogenization and comparison with alternative homogenization methods, *Int. J. Mech. Sci.* 77 (2013) 249–262.
 - [34] O.L.A. Harrysson, O. Cansizoglu, D.J. Marcellin-Little, D.R. Cormier, H.A. West li, Direct metal fabrication of titanium implants with tailored materials and mechanical properties using electron beam melting technology, *Mater. Sci. Eng. C* 28 (2008) 366–373.
 - [35] S. Van Bael, G. Kerckhofs, M. Moesen, G. Pyka, J. Schrooten, J.P. Kruth, Micro-CT-based improvement of geometrical and mechanical controllability of selective laser melted Ti6Al4V porous structures, *Mater. Sci. Eng. A* 528 (2011) 7423–7431.
 - [36] V. Deshpande, M. Ashby, N. Fleck, Foam topology: bending versus stretching dominated architectures, *Acta Mater.* 49 (2001) 1035–1040.
 - [37] A. Vigliotti, D. Pasini, Linear multiscale analysis and finite element validation of stretching and bending dominated lattice materials, *Mech. Mater.* 46 (2012) 57–68.
 - [38] L.J. Gibson, M.F. Ashby, *Cellular Solids: Structure and Properties*, Cambridge University Press, Cambridge, UK, 1999.
 - [39] M.S.A. Elsayed, D. Pasini, Multiscale structural design of columns made of regular octet-truss lattice material, *Int. J. Solids Struct.* 47 (2010) 1764–1774.
 - [40] V. Deshpande, N. Fleck, M. Ashby, Effective properties of the octet-truss lattice material, *J. Mech. Phys. Solids* 49 (2001) 1747–1769.
 - [41] A. Vigliotti, D. Pasini, Stiffness and strength of tridimensional periodic lattices, *Comput. Methods Appl. Mech. Eng.* 229–232 (2012) 27–43.
 - [42] A. Vigliotti, D. Pasini, Mechanical properties of hierarchical lattices, *Mech. Mater.* 62 (2013) 32–43.
 - [43] A. Vigliotti, V.S. Deshpande, D. Pasini, Non linear constitutive models for lattice materials, *J. Mech. Phys. Solids* 64 (2014) 44–60.
 - [44] L. Mullen, R. Stamp, P. Fox, E. Jones, C. Ngo, C. Sutcliffe, Selective laser melting: a unit cell approach for the manufacture of porous, titanium, bone in-growth constructs, suitable for orthopedic applications. II. Randomized structures, *J. Biomed. Mater. Res. Part B: Appl. Biomater.* 92 (2009) 178–188.
 - [45] S.J. Hollister, Porous scaffold design for tissue engineering, *Nat. Mater.* 4 (2005) 518–524.
 - [46] H. Kang, C.Y. Lin, S.J. Hollister, Topology optimization of three dimensional tissue engineering scaffold architectures for prescribed bulk modulus and diffusivity, *Struct. Multidiscip. Optim.* 42 (2010) 633–644.
 - [47] M.S.A. Elsayed, D. Pasini, Analysis of the elastostatic specific stiffness of 2D stretching-dominated lattice materials, *Mech. Mater.* 42 (2010) 709–725.
 - [48] M. Goldberg, Three infinite families of tetrahedral space-fillers, *J. Comb. Theory Ser. A* 16 (1974) 348–354.
 - [49] J.E. Lemons, Quantitative Characterization and Performance of Porous Implants for Hard Tissue Applications: A Symposium, ASTM International, 1987.
 - [50] A.C. Jones, C.H. Arns, A.P. Sheppard, D.W. Huttmacher, B.K. Milthorpe, M.A. Knackstedt, Assessment of bone ingrowth into porous biomaterials using MICRO-CT, *Biomaterials* 28 (2007) 2491–2504.
 - [51] C. Lin, J. Miller, Network analysis of filter cake pore structure by high resolution X-ray microtomography, *Chem. Eng. J.* 77 (2000) 79–86.
 - [52] V. Karageorgiou, D. Kaplan, Porosity of 3D biomaterial scaffolds and osteogenesis, *Biomaterials* 26 (2005) 5474–5491.
 - [53] I. Yadroitsev, I. Shishkovsky, P. Bertrand, I. Smurov, Manufacturing of fine-structured 3D porous filter elements by selective laser melting, *Appl. Surf. Sci.* 255 (2009) 5523–5527.
 - [54] E. Abele, H.A. Stoffregen, M. Kniepkamp, S. Lang, M. Hampe, Selective laser melting for manufacturing of thin-walled porous elements, *J. Mater. Process. Technol.* 215 (2015) 114–122.
 - [55] Normalisation Old, Standardization IOF, ISO 13314: ISO, 2011.
 - [56] S. McKown, Y. Shen, W. Brookes, C. Sutcliffe, W. Cantwell, G. Langdon, et al., The quasi-static and blast loading response of lattice structures, *Int. J. Impact Eng* 35 (2008) 795–810.
 - [57] C. Yan, L. Hao, A. Hussein, D. Raymont, Evaluations of cellular lattice structures manufactured using selective laser melting, *Int. J. Mach. Tools Manuf.* 62 (2012) 32–38.
 - [58] C. Yan, L. Hao, A. Hussein, P. Young, D. Raymont, Advanced lightweight 316L stainless steel cellular lattice structures fabricated via selective laser melting, *Mater. Des.* 55 (2014) 533–541.
 - [59] G. Pyka, A. Burakowski, G. Kerckhofs, M. Moesen, S. Van Bael, J. Schrooten, et al., Surface modification of Ti6Al4V open porous structures produced by additive manufacturing, *Adv. Eng. Mater.* 14 (2012) 363–370.
 - [60] L. Mullen, R.C. Stamp, P. Fox, E. Jones, C. Ngo, C.J. Sutcliffe, Selective laser melting: a unit cell approach for the manufacture of porous, titanium, bone in-growth constructs, suitable for orthopedic applications. II. Randomized structures, *J. Biomed. Mater. Res. Part B: Appl. Biomater.* 92B (2010) 178–188.
 - [61] L.D. Zardiackas, D.E. Parsell, L.D. Dillon, D.W. Mitchell, L.A. Nunnery, R. Poggie, Structure, metallurgy, and mechanical properties of a porous tantalum foam, *J. Biomed. Mater. Res.* 58 (2001) 180–187.
 - [62] L.L. Hermansen, M. Sørensen, J. Barckman, J.E. Bechtold, K. Søballe, J. Baas, Incorporation of raloxifene-impregnated allograft around orthopedic titanium implants impairs early fixation but improves new bone formation: a 4-week study in 12 dogs, *Acta Orthopaedica* 85 (2014) 1–7.
 - [63] S.R. Frenkel, W.L. Jaffe, F. Dimaano, K. Iesaka, T. Hua, Bone response to a novel highly porous surface in a canine implantable chamber, *J. Biomed. Mater. Res. B Appl. Biomater.* 71 (2004) 387–391.
 - [64] M. Doyoyo, J.W. Hu, Multi-axial failure of metallic strut-lattice materials composed of short and slender struts, *Int. J. Solids Struct.* 43 (2006) 6115–6139.